

# ON THE DEVELOPMENT OF DUAL GRAPHITE IRON AS A FUNCTIONALLY GRADED MATERIAL

S. Boonmee  and S. Rassamipat

Suranaree University of Technology, Nakhon Ratchasima, Thailand

Copyright © 2023 American Foundry Society  
<https://doi.org/10.1007/s40962-023-01023-8>

## Abstract

Graphite morphology plays significant roles in mechanical properties in graphitic cast irons. Typically, cast irons are made with uniform graphite morphology and distribution across the microstructure of castings. This research explored the possibility of using the difference in graphite morphology over the volume of castings to create a Functionally Graded Material (FGM). The FGM will enable future applications that require the tailor-made microstructure. The hybridization method used in this research was the sulfurization of liquid iron using the sulfur-bearing cores. The result was the Dual Graphite Iron (DGI) that comprised with the lamellar and spheroidal graphite (LG and SG). It was found that the thickness

of LG layer increased with increasing sulfur levels in cores. The maximum thickness of the LG layer of 2.2 mm was observed at 6.6 wt%S. The LG/SG interfaces were quite smooth (e.g., controllable) up to 8.8 wt%S where the scattering of the LG microstructure appeared. It was concluded that sulfurization of liquid iron was viable method for producing DGI.

**Keywords:** dual graphite iron, functionally graded materials, ductile iron, casting skin, graphite degradation, sulfurization method, hybridization

## Introduction

Previous studies showed that the subsurface microstructure in ductile iron castings could differ from the bulk microstructure depending on the casting parameters. The differences are including the graphite morphology and the matrix structures. Several investigators<sup>1,2</sup> reported the occurrence of the lamellar graphite layer near the casting surface which leads to the negative impact on the mechanical properties (e.g., tensile strength, fatigue strength). The lamellar graphite layer is known as the “graphite degradation layer” which is a subsurface feature of the casting skin. Figure 1 shows an example micrograph of the graphite degradation layer. It is seen that the graphite degradation layer is observed next to the casting surface. The main formation mechanisms of the casting skin were magnesium depletion and sulfurization via molding materials.<sup>3</sup> There have been studies on minimizing the occurrence of the graphite degradation layer via mold coatings. It was reported that the MgO coating was able to reduce the

thickness of the graphite degradation layer.<sup>4-6</sup> This confirmed that the sulfurization is the main formation mechanism of the phenomenon. Furthermore, Ivan et al.<sup>5</sup> suggested that a reactive coating of Mg-FeSi materials contribute to the Mg replenishment which further reduced the graphite degradation layer.

Functionally Graded Materials (FGMs) are materials with variations of chemical composition, microstructures, and properties over volume of the parts. Previously, FGMs were mainly made by combining materials from different families (e.g., ceramics, polymers, metals) to form composite materials. However, typical composite materials exhibit an abrupt change in microstructure and properties which sometimes suffer from the delamination when subjected to thermal or mechanical fatigue.<sup>7</sup> On contrary, the FGMs have gradual transition of changes and do not prone to fatigue.<sup>8</sup> The examples of FGMs fabrication processes are including powder metallurgy, centrifugal casting, and vapor deposition method. In fact, FGMs can be found in nature as well. Bones have denser structure near the surface providing wear resistance and strength. On the other hand, bones are less dense in the central part resulting in the

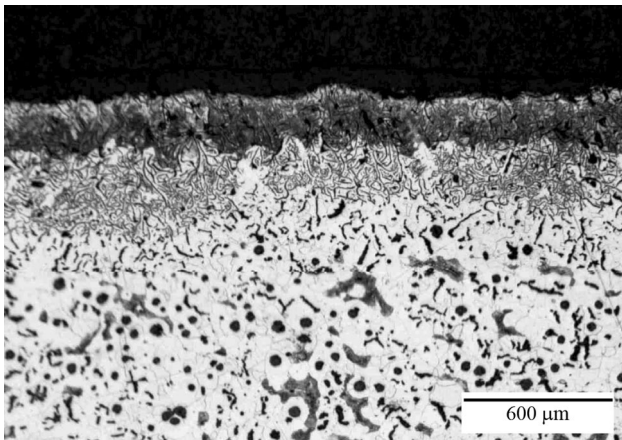


**Figure 1. Examples of the graphite degradation layer in ductile iron.**

better specific strength. The study of design using the inspiration by nature is called “biomimicry”. Assuming that nature has been going through iterations of designs over million years, many designs by nature are the clever ways to use the materials and inspired by designers.<sup>9</sup>

FGMs can be created with metalcasting processes. There have been number of studies that created FGMs using the centrifugal casting.<sup>10</sup> Distribution of reinforcement particles can be engineered by adjusting casting parameters such as rotating speed and solidification rate. A review on these works can be found in Reference 10. For conventional casting processes, some studies focused on engineering the casting surfaces to achieve desirable properties such as wear resistance and corrosion resistance. Rane et al.<sup>11</sup> developed a method to improve hardness and corrosion resistance of a steel component using a metal powder mold coating. The results showed the formation of the surface alloyed layer containing Ni, Cr, Si and Mn which provided lower corrosion rate and higher hardness than the base WCB steel. A similar approach by El Fawkhry et al.<sup>12</sup> was the mold coating of silicon carbide and ferrochromium for low alloy steel. This led to the formation of the silicon and chromium carbide particles near the casting surface which resulted in better wear resistance than the base steel (AISI 1020). A recent study by Wróbel et al.<sup>13</sup> used the additive manufacturing in cooperate with sand casting to create a FGM. Gray iron was poured in mold cavities with 3D printed spatial skeleton Ti inserts. Titanium carbide particles were observed in an area adjacent to the inserts providing better wear resistance. The application of additive manufacturing to create FGMs could gain more attention in future.

Cast iron is one of the most commonly used engineering material. Since cast irons have lowest cost per unit mass (or volume) among engineering alloys; therefore, they have been used in wide range of applications. The main drawback of cast irons is the lower specific strength when

compared to the lightweight alloys. Microstructure of gray and ductile irons consists with graphite particles and the iron matrix which can be considered as a composite structure. Therefore, variation of graphite morphology and fraction over the volume of a casting can be considered as an FGM. This infers that the performance of cast iron can be further increased by having the appropriate graphite morphology at the location that requires specific properties. One excellent example was demonstrated by Malizio and Jennings.<sup>14</sup> In the patent, it was claimed that the gray iron pipe has better corrosion resistance than ductile iron and steel pipes for transporting 95% sulfuric acid at elevated temperature (120–150 °C). The interconnected lamella graphite in gray iron inhibits the propagation of corrosion (*a.k.a.* self-corrosion inhibition). On contrary, the spheroidal graphite particles are isolated and do not have similar effect to the gray iron counterpart. Therefore, a pipe for specific types of corrosive chemicals can be made with the lamellar graphite on the interior for corrosion resistance and the spheroidal graphite on the exterior for strength. It is worth noting that the corrosion behavior of the gray and ductile iron can be different depending on the corrosive media and conditions. As seen, the differences in graphite morphology and fraction can be altered to achieve the desirable properties at various locations in the castings. Another potential application is the engine block. The lamellar graphite in gray irons promotes damping capacity and thermal conductivity whereas the spheroidal graphite gives the strength and ductility in ductile irons. Engine blocks require both thermal conductivity for heat dissipation, damping capacity for noise reduction and strength for the structural integrity. The present solution for the engine blocks is the compacted graphite iron (CGI). The further development is the hybridization of the graphite types across the casting. Presumably, having the lamellar graphite at the locations where heat dissipation is needed and having spheroidal graphite where strength is required would give the optimal solution to such applications. Present study focuses on the hybridization of cast iron microstructure as an FGM.

There have been studies regarding the dual graphite (DG) iron. Martin and Karsay<sup>15</sup> found that localized lamellar graphite could form at casting surface. This is due to the reaction between molten metal and molding materials. Several investigators reported the negative effect of the casting skin on mechanical properties. Approximately 10 and 40 percent of reduction of tensile and fatigue strength were reported, respectively.<sup>1</sup> Nasu et al.<sup>16</sup> reported that the test sample from green sand molds showed ferrite colonies on the casting surface. The combination of the graphite degradation layer and the ferrite colonies contributed to approximately 30% reduction of the fatigue strength despite the finer eutectic cell in the samples. As for development of the DG iron, the method for fabrication of the dual graphite structured pipe was filed by Malizio and Jennings in 1989.<sup>14</sup> The invention claimed that the

**Table 1. Summary of Previous Studies on Development of DG Iron**

	Experimental Approach	References
Malizio and Jennings (1989)	Double pouring with different melt composition in centrifugal casting; pipe shape	14
Lekakh et al. (2012)	(i) In-ladle FeS <sub>2</sub> treatment; stationary molds (ii) Intermittent in-stream FeS <sub>2</sub> treatment; stationary tundish; moving molds (iii) Similar to ii) but with different design (plate with a core, bottom gate) (iv) Double pouring; plate casting with cores; multiple side gates	17
Boonmee and Mai-Ngam (2013)	Rectangular block casting; multiple sulfur-bearing cores; single pouring of Mg treated melt	18
Kutz et al. (2020)	Multiple rectangular plates; sulfur-bearing cores on the bottom surfaces	19

connected network of lamellar graphite provides the self-inhabitation property. The method involving with double pouring in centrifugal casting process. Lekakh et al.<sup>17</sup> attempted to produce dual graphite structure in castings by various approaches such as partial melt treatment, sequential fill with different melt composition. The result showed that the processes were rather challenging. Boonmee and Mai-Ngam<sup>18</sup> used sulfur-bearing cores placed in the middle of castings the generate the graphite degradation layer around the cores. The study showed that the higher levels of sulfur resulted in thicker graphite degradation layer. However, there were difficulties in the controlling of the formation of the layers due the convection of liquid iron and the graphite flotation. Kutz et al.<sup>19</sup> experimented with the adjustment of the formation of the graphite degradation layer to produced fatigue test samples with the presence of the casting skin. It was found that the conventional furan resin did not produce the intended thickness (500 μm) of the graphite degradation layer. Furthermore, they concluded that using pyrite or sulfur powders demonstrated the most promising results. Table 1 summarizes the previous studies on developing DG iron.

## Experimental Procedure

### Test Casting Design

A test casting was designed specifically for this experiment. The design criteria are as follows.

- The design must provide the placement of multiple sulfur-bearing cores. These cores will be used at the source of sulfur for melt treatment.
- Mold cavity must be filled with the minimal turbulence. Convection on the core surface will result in uncontrollable of the occurrence of lamellar graphite.
- The test casting must provide a comparable cooling rate to the typical industrial counterpart.

In order to fulfill the design requirements, the commercial casting simulation software was used to determine the

filling pattern, velocity at the gate, temperature distribution and cooling rate.

Figure 2 shows the design used in this study. The sulfur-bearing cores were place at the top of each cavity providing minimal melt convection. The design allowed 6 samples with different sulfur levels in one casting. The simulated velocity at the gate was in the range of 0.18–0.27 m/s which was acceptable. The simulated cooling rate (5 °C before the eutectic reaction) was approximately 0.75°C /s at 5 mm from the top surface.

The molds used were green sand. The molding sand used was silica sand with GFN 55–60. Cores were made of silica sand and ferrosulfur with sodium silicate as a binder.

### Production of the Test Casting

Two iron heats were produced using an induction furnace (60kW, 100-kg capacity). The melting cycles included superheating at 1620 °C to minimize pre-existing nuclei and then tapped at 1550–1570 °C. The pouring temperature was 1470 ± 10 °C. To observe the influence of processing parameters, no inoculation was done to the melt which can obscure the influence in the as-cast microstructure.

In present study, the sulfurization method was used as it is more controllable and has less limitation than other approaches. The design of test casting is shown in Figure 2. As seen the design consists with six mold cavities (50 × 50 × 50 mm). Sulfur-bearing cores were placed at the top of cavities. There were two types of sulfur-bearing cores. The first type was achieved by mixing the ferrosulfur with sodium silicate sand and then exposed with carbon dioxide. The levels of sulfur in cores were 0, 4.4, 6.6, 8.8 and 11.0 wt%S. The latter type was sodium silicate core coated with a sulfur-bearing mold wash (alcohol-based alumina mixed with ferrosulfur). The ferrosulfur used was 20–45 microns in size. The coating thickness was approximately 500 μm throughout the experiment. The level of sulfur in the coatings were 0, 4.4, 6.6, 8.8 and 11.0 wt%S. The

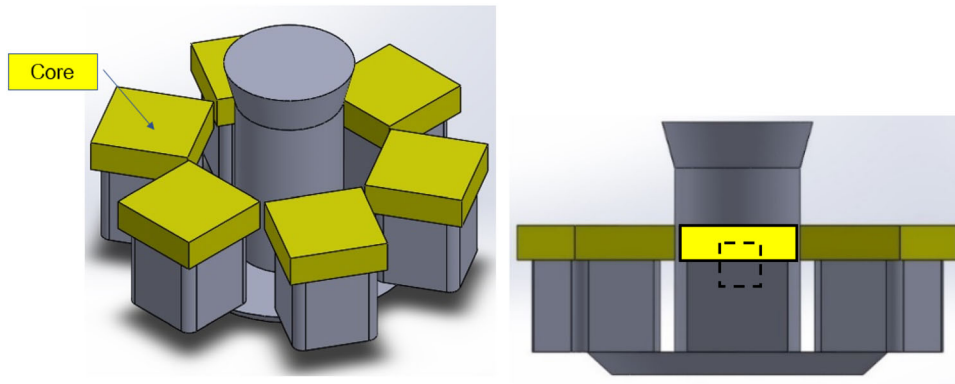


**Figure 2. The design of test casting in present study.**

ferrosulfur used contained 44 wt%S. It is worth noting that this design employed the bottom gates for the quiescent filling. The filling pattern is rather important as sulfur could be washed by liquid iron resulting in irregular results. The castings were then dissected for microscopic examination at the middle of top surface (adjacent to the cores).

### Characterization

The quantification of the graphite morphology (*e.g.*, graphite shape factors) was done under an optical microscope and an image analysis software. Several shape factors were used such as Roundness, Circularity and Aspect ratio. Table 2 summarizes the formulae and definitions of shape factors used in this study.

To measure the thickness of lamellar graphite layer ( $T_{LG}$ ), the line at the LG-to-SG transition boundary was established. Then the perpendicular lines from the casting surface to the boundary were drawn. The average of the length of the lines ( $y_i$ ) was calculated for the thickness of lamellar graphite layer ( $T_{LG}$ ) with the following equation.

$$T_{LG} = \frac{\sum_i^n y_i}{n}$$

Another parameter included in the analysis is tortuosity ( $\Omega$ ). The tortuosity measures the curviness of the LG-to-SG boundary which is important from the development of DG iron perspective. The tortuosity is calculated by the following equation.

$$\Omega = \frac{C}{L}$$

where  $C$  is the length of LG-to-SG boundary and  $L$  is the width of image frame. Figure 3 demonstrates the measuring method for  $T_{LG}$  and  $\Omega$ .

Color metallurgy was applied to a selected sample, the etchant used was 80 g of NaOH, 20 g of KOH, 20 g of

**Table 2. Summary of Formulae and Definitions of Graphite Shape Factors**

Quantity	Equation	Definition
Circularity	$C = 4\pi \frac{A}{P^2}$	$P$ : perimeter of graphite particle $A$ : Area of a graphite particle
Roundness	$R = \frac{4A}{\pi r^2}$	$r$ : radius of circumscribed circle
Aspect ratio	$A_{ratio} = \frac{l_{max}}{l_{min}}$	$l_{max}$ : Length of longest ferret $l_{min}$ : Length of shortest ferret
Graphite fraction	$f_{Gr} = \frac{A_{Gr}}{A_{total}}$	$A_{Gr}$ : Total area of graphite $A_{total}$ : Total area of image

picric acid in 200 ml of distilled water. The samples were immersed in the etchant at 120 C for 120 seconds.

The Electron Probe Micro Analysis (EPMA) was done to a selected sample with 8.8 wt%S coated in cores. Both mapping and line scanning were done with the beam size of

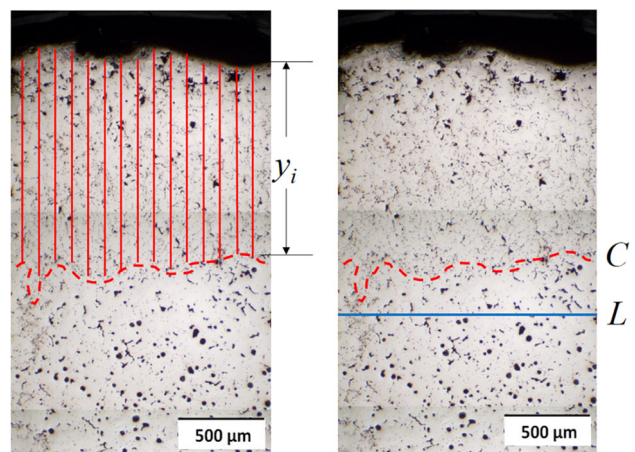


**Figure 3. The representation for the measurement of the thickness of LG-to-SG boundary layer ( $T_{LG}$ ) and the tortuosity ( $\Omega$ ).**

1  $\mu\text{m}$ . Measuring time (*a.k.a.* dwell time) was 10 milliseconds. The accelerating voltage was 15 kV.

The surface roughness was measured by a stylus roughness tester with a capacity up to 30 microns.

## Results and Discussions

### Chemistry

Table 3 shows the chemical composition of treated melts. It is seen that the carbon equivalents were 4.24 and 4.60 for Heat I and Heat II, respectively. This was intentional to observe the difference in the precipitation of the primary phases (primary austenite vs. primary graphite) in the hypoeutectic and hypereutectic irons. Despite the low level of magnesium (0.031–0.035%Mg), the overall visual nodularity in the bulk microstructure was still greater than 80%. In fact, the higher Mg level than this could affect the desired thickness of the graphite degradation layer.

### Microstructure

Figures 4 and 5 show a microstructure of the test castings without the sulfur-bearing cores for hypoeutectic and hypereutectic composition, respectively. The casting surfaces (next to the cores) were to the far left of the images. It is seen that both samples were absence of the graphite degradation layer. This indicates that with this level of Mg/S ratio the ductile iron can be produced without concern of the casting skin effect. Furthermore, the hypereutectic condition showed the large graphite nodules scattered throughout the microstructure. This is known as the graphite flotation commonly occurred in the hypereutectic iron with the improper or without inoculation. The visual nodularity was greater than 80% for both conditions. The nodule counts were 266.5 and 152.4 nodules/mm<sup>2</sup> for the hypoeutectic and the hypereutectic conditions, respectively. The hypoeutectic iron demonstrated lower graphite fraction (0.09, by area) as compared to the hypereutectic iron (0.14), which was expected from the difference in the carbon equivalents.

Figure 6 shows example microstructures of hypoeutectic and hypereutectic SG irons with 8.8 wt%S-mixed cores. It can be seen that the layers of graphite degradation were found adjacent to the casting surface. For the hypoeutectic iron, sulfur from core diffused through the molten iron and reacted with magnesium resulting in low Mg/S zone. Consequently, the available sulfur and oxygen promoted

the formation of lamellar graphite. This phenomenon occurred from the casting surface to the location where the level of Mg/S increased back to the normal range (in this case  $\sim 1,800 \mu\text{m}$ ). As a result, the transition in the graphite morphology from the lamellar graphite (LG) to the spheroidal graphite (SG) was observed. For the hypereutectic iron, the primary graphite was the first phase to form. Some nodules of the primary graphite floated to the top of the casting. Thus, the nodules coexisted with lamellar graphite in the low Mg/S zone. Noted that the casting surface quality was relative poor and unmeasurable by a surface roughness tester (over 30 microns). The introduction of ferrosulfur in the cores reduced the refractoriness of the molding sand; hence, greater degree of metal penetration was observed. At higher magnification, the difference in the presence of the nodular graphite in the hypoeutectic and the hypereutectic irons can be seen in Figure 7. As seen the nodules are encapsulated by the austenite for the hypoeutectic iron where the nodules in the hypereutectic iron were not. In addition, the graphite morphology changed over distance from the casting surface (Figure 8). For hypoeutectic DG iron, the roundness ( $R$ ) and circularity ( $C$ ) showed low values at the casting surface and increased with distance up to the location of the LG-to-SG transition. On contrary, the aspect ratio ( $A_{\text{ratio}}$ ) decreased with distance from the casting surface up to the transition. At the transition, values of  $R$  and  $C$  changes markedly with distance from surface. Typically, peaks of graphite shape factors ( $R$  and  $C$ ) were observed after the LG-to-SG transition due to the combination effect of sulfurization and cooling rate. After the peak, the graphite shape factors ( $R$  and  $C$ ) decreased toward the center of the cross section. These observations were in line with previous study.<sup>3</sup> For the hypereutectic DG iron, the effect was not as clear as the hypoeutectic counterpart because of the effect of the graphite flotation. Therefore, the hypereutectic compositions were not pursued for in the further experiments. These observations were consistently found in all conditions in this study.

Figure 9 shows the microstructure of the hypoeutectic DG iron with 4.4, 6.6, 8.8, 11.0 and 13.2 wt%S-mixed cores. It is seen that the thickness of the lamellar graphite layer increased with the level of sulfur up to 2,151  $\mu\text{m}$  at 6.6 wt%S. This was expected as the higher level of sulfur in the mixed cores created the higher sulfur concentration gradient resulting in the higher diffusion rate of sulfur in the liquid iron. In addition, the higher level of sulfur in the mixed cores provided greater available sulfur for diffusion. At higher level of sulfurs (*e.g.*, 8.8 and 11.0 wt%S); however, the thickness of the lamellar graphite layer decreased. This can be explained through the chilling effect

**Table 3. Chemical Composition of the Treated Melts**

	C	Si	Mn	P	S	Cu	Mg	C.E	Mg/S
Heat I	3.46	2.34	0.44	0.041	0.017	<0.05	0.031	4.24	1.85
Heat II	3.68	2.77	0.41	0.042	0.017	<0.05	0.035	4.60	2.06

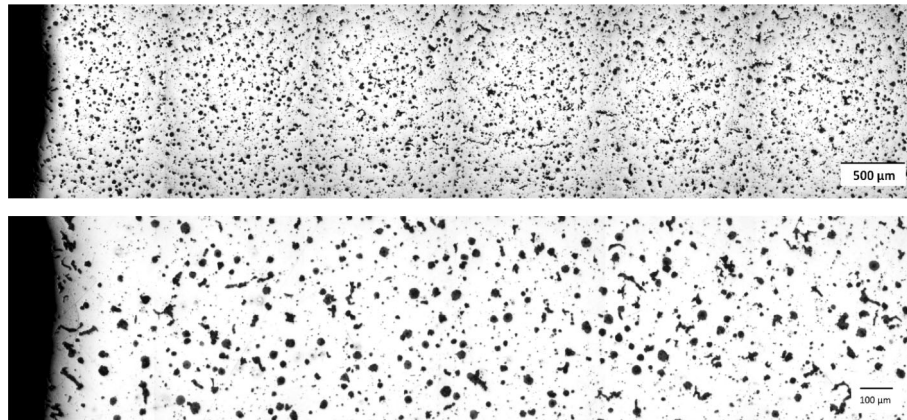


**Figure 4. Microstructure of hypoeutectic SG iron (Heat I) without sulfur-bearing core.**

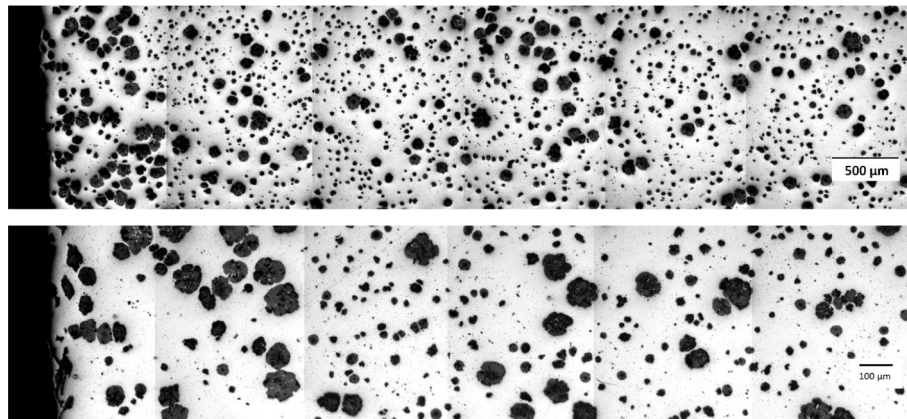


**Figure 5. Microstructure of hypereutectic SG iron (Heat II) without sulfur-bearing core.**

of the ferrosulfur in the cores. As the ferrosulfur content increased, heat in liquid iron was absorbed and used for the melting of the ferrosulfur. As a result, the solidification time of liquid iron was reduced; hence, the diffusion of sulfur is demoted. Figure 10 shows the thickness of the lamellar graphite layer ( $T_{LG}$ ) for various percent sulfur in mixed cores. At 13.2 wt% S, the double layers of lamellar graphite were observed. Presumably, the layer of early solidified LG iron was shrunk and drawn away from the liquid metal-core interface allowing the liquid iron to seep in the gap. Therefore, the final microstructure showed double LG layers. The other explanation was flaking off of the sulfur-mixed core. However, this was unlikely as no

sand inclusion was found in all conditions. Nonetheless, the occurrence of the double LG layer was not consistent as seen in the error bar depicted in Figure 10. Figure 11 shows the effect of the level of sulfur in mixed cores on the tortuosity ( $\Omega$ ). The value of the tortuosity demonstrated the curviness of the LG layer whereas the perfect smooth layer returns the value of 1.0. As seen, the observed tortuosity appears to be in line with the  $T_{LG}$ . The greater  $T_{LG}$  resulted in higher tortuosity and vice versa.

Figure 12 shows the microstructure of hypoeutectic DG iron with 4.4, 6.6, 8.8, 11.0 and 13.2 wt% S-coated cores. The similar trend to the mixed core counterpart was seen.

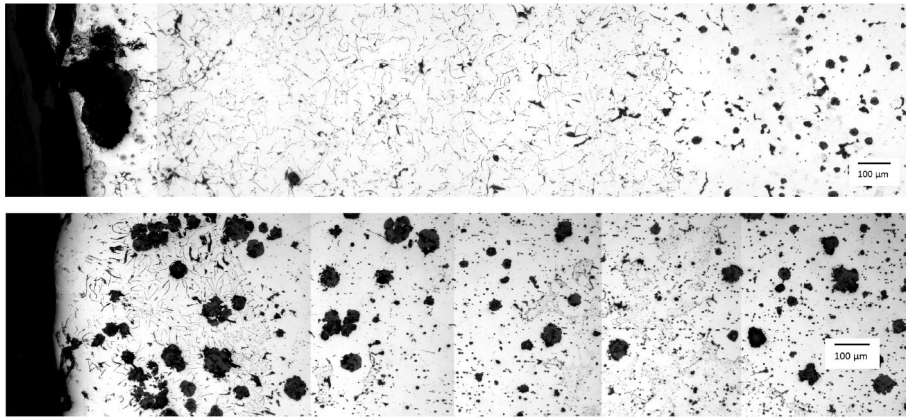


**Figure 6. Microstructure of hypoeutectic (Heat I) and hypereutectic (Heat II) DG iron with 8.8 wt%S-mixed cores.**

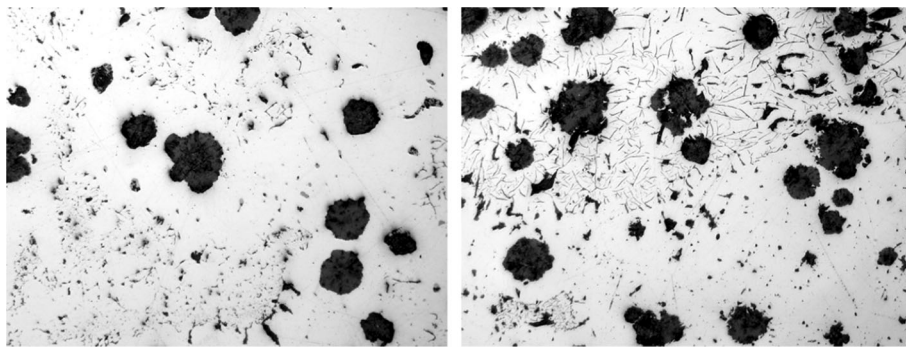


**Figure 7. Presence of nodular graphite in hypoeutectic (left) and hypereutectic (right) DG irons.**

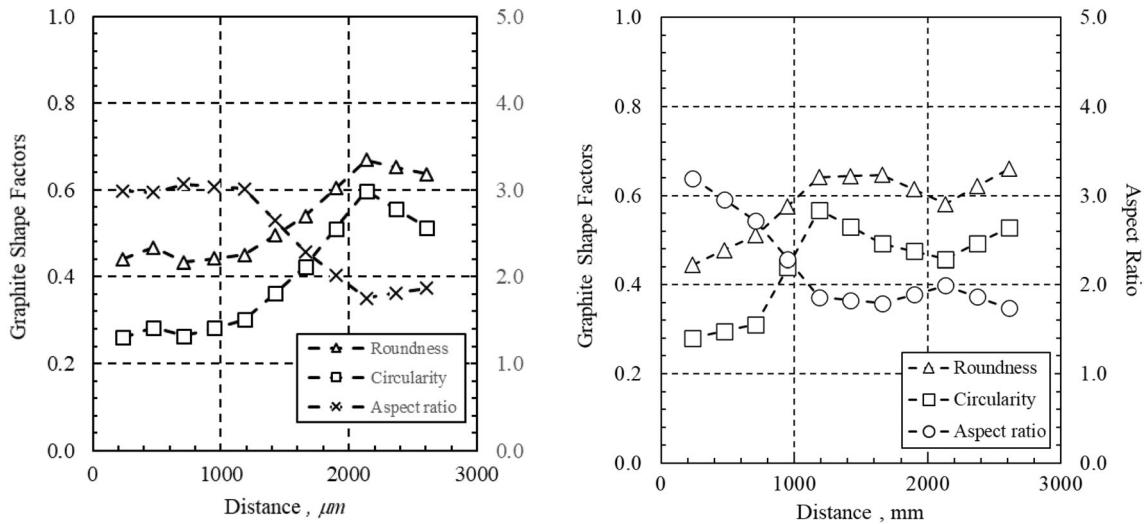


**Figure 8. Graphite shape factors as function of distance from the casting surface in hypoeutectic (left) and hypereutectic (right) DG iron with 6.6 wt%S-mixed cores.**

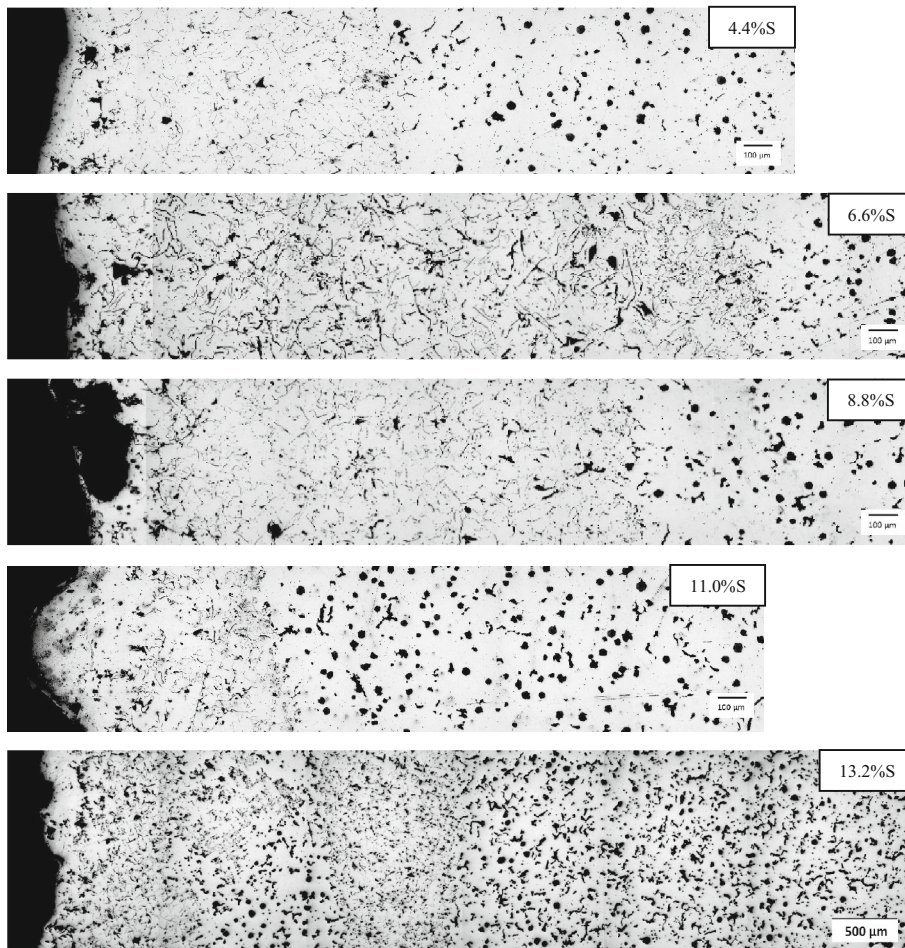


**Figure 9. Microstructure of hypoeutectic DG iron with various levels of sulfur in the mixed cores.**

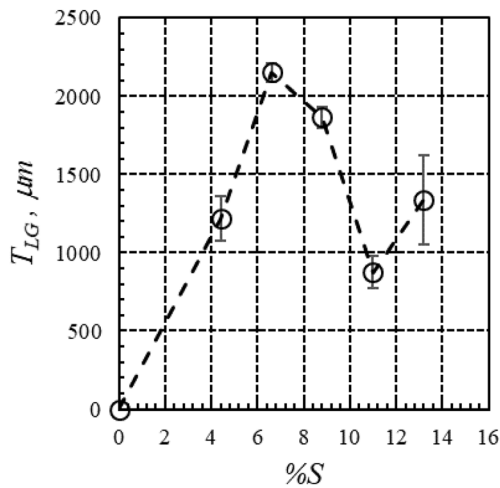


**Figure 10. Thickness of the lamellar graphite layer ( $T_{LG}$ ) at various level of sulfur in the mixed cores.**

The thickness of the lamellar graphite layer ( $T_{LG}$ ) for various percent sulfur in the coated cores is shown in Figure 13. Notable differences in results between types of sulfur-bearing cores were (i) the  $T_{LG}$  in the coated core was lower at the same level of sulfur; (ii) the surface quality of

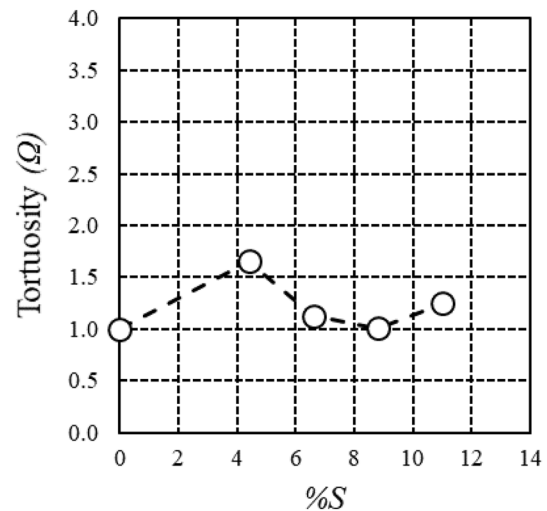


**Figure 11. Tortuosity ( $\Omega$ ) at various level of sulfur in the mixed cores.**

castings of the coated cores was noticeably improved. Presumably, the coated cores produced smaller  $T_{LG}$  because of the available sulfur atoms were fewer than the mixed cores. Figure 14 shows the comparison of surface



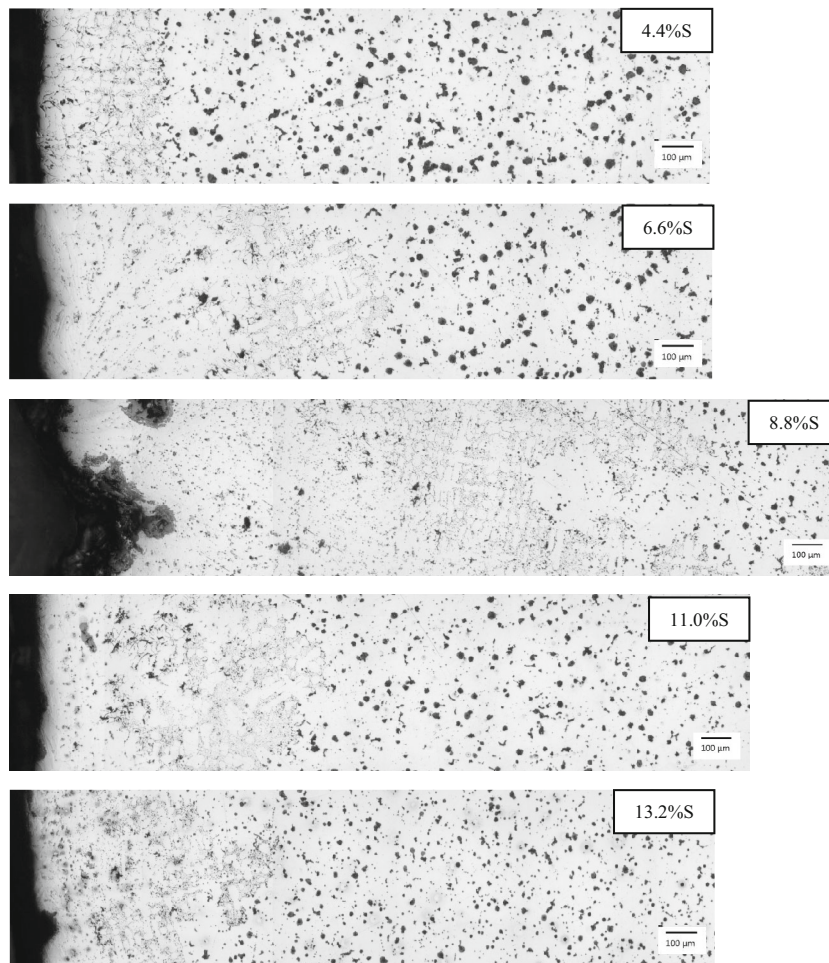


**Figure 12. Microstructure of hypoeutectic DG iron with various levels of sulfur in the coated cores.**

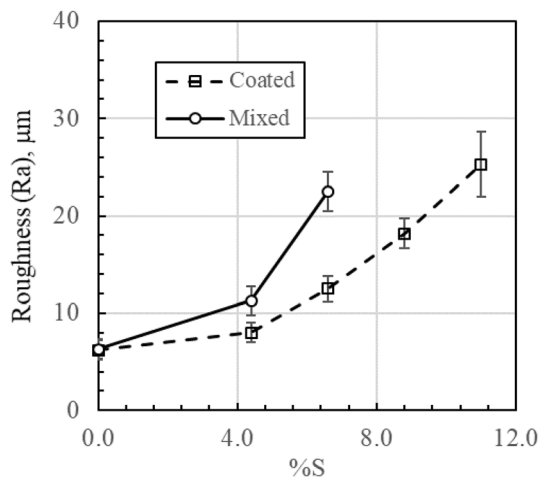


**Figure 13. Comparison of the surface roughness of the test samples with mixed and coated cores.**

roughness between the mixed and coated cores. It is seen that the coatings have higher refractoriness than the mixed core resulting in the better surface quality. In fact, the mixed cores demonstrated severe roughness at higher than

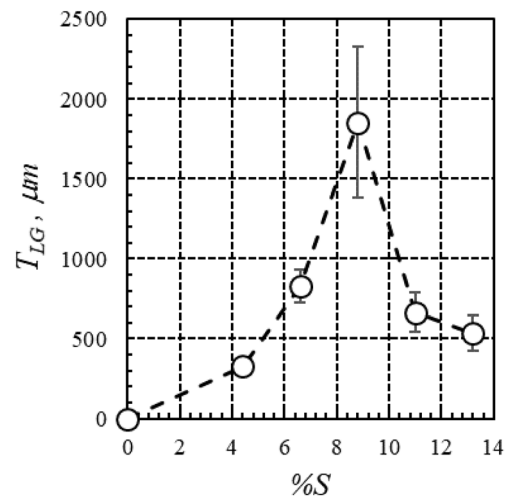


**Figure 14. Thickness of the lamellar graphite layer ( $T_{LG}$ ) at various level of sulfur in the coated cores.**

8.8 wt%S that were unmeasurable by the roughness tester. For the coated cores, some severe roughness were found at the higher level of sulfur in the coated cores. This could be the result from the presence of the agglomeration of the

ferrosulfur particles in the coating. Figure 15 shows the tortuosity of the LG layer ( $\Omega$ ) for various percent sulfurs in the coated cores. It was seen that the conditions with the thicker LG layer produced higher tortuosity. This demonstrates the nature of the random walk in the diffusion process. In addition, the double LG layers were found in the samples from the coated cores. This was explained by the following steps. Firstly, the liquid iron at mold/metal interface is sulfurized and became LG layer upon solidification. Secondly, the layer occasionally fell off from the mold/metal interface because of the higher density of the solidified metal (i.e., natural convection). The new liquid metal then replace the space and solidified with SG structure because of the limited available sulfur in the coatings

(unlike the mixed core counterpart). As a result, the SG-LG-SG structures were found occasionally at 13.2 wt%S. Figure 16 demonstrates the formation mechanisms of the double LG layers. The double LG layer occurred only in the anti-gravity direction (top surface). To explore the nature of the double LG layer in greater extent, a selected sample was color etched to reveal the segregation of elements in the microstructure. The contrast in the color metallography was created by the solute segregation within the microstructure. The brighter (bluish) area in Figure 17 was higher in silicon and lower in manganese and vice versa for the darker (orangish) area. It is seen that the cellular structure at the double LG layer and the dendritic structure at the SG layer. This demonstrates the cooperative and divorced eutectic growth mechanisms for the LG and SG layer, respectively.

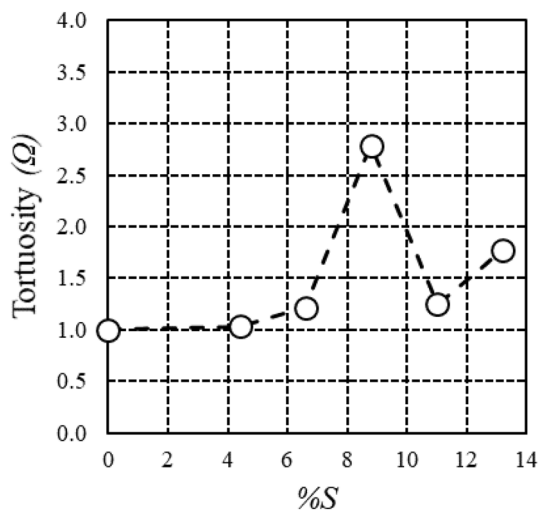


**Figure 15. Tortuosity ( $\Omega$ ) at various level of sulfur in the coated cores.**

### Electron Probe Microanalysis (EPMA)

For better understanding of metallurgical phenomena of the hybridization, a selected sample was further analyzed with EPMA technique. Figure 18 shows the solute segregation in the LG-SG transition area of the sample with 8.8 wt%S-coated core. As expected, the carbon-rich and silicon-rich areas were coincide with the graphite and iron matrix, respectively (Figure 18b, c). Manganese was uniformly scattered in the LG layer where the MnS particles resided. In addition, manganese and phosphorus were found at the interdendritic area in the SG structure (Figure 18d, e). As expected, sulfur was found mainly near the casting surface where the LG layer located. Magnesium was distributed mainly next to the core representing the MgS and MgO.

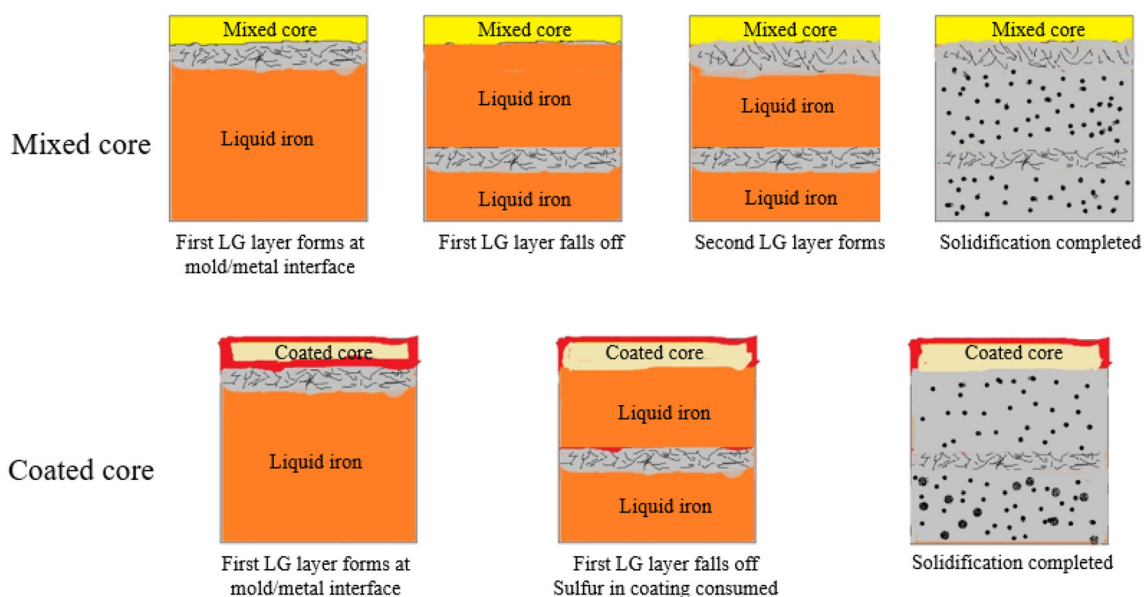


**Figure 16. Formation mechanism of the double LG layer occurrence in DG iron with sulfur-mixed and coated cores.**

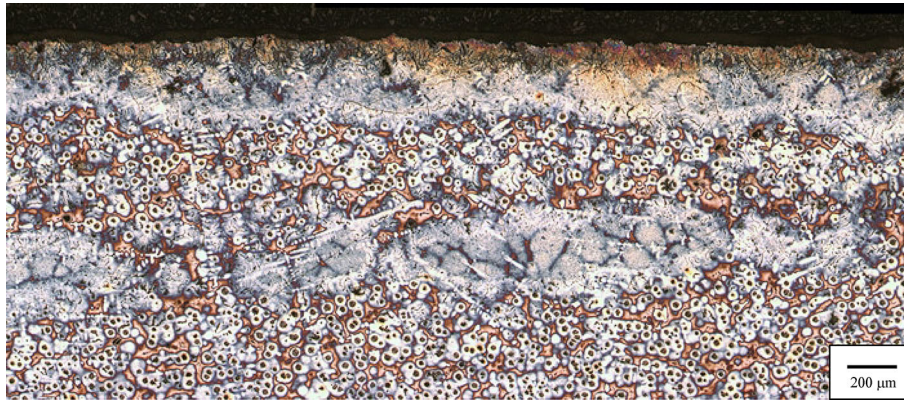
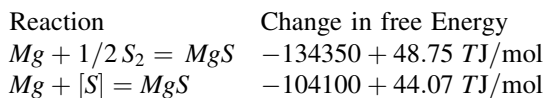


**Figure 17. Color-etched microstructure of the double LG layer.**

Further analyses were done with the line scanings of elements across the LG-SG transition. As seen in Figure 19a, the carbon content were widely varying throughout the scanning. This was expected as the scanning was through graphite particles or the matrix which return very high and very low signals, respectively. For phosphorus, there was a peak at the LG-SG transition (Figure 19b). This was due to the solute redistribution of phosphorus in the solidified structure. When consider the Fe-P phase diagram, the relatively low value of the partition coefficient was observed (0.20–0.25). The signal of phosphorus was peaked at the LG-SG transition and gradually decreased to an average value of 0.04. The thickness of the boundary layer was about 1 mm. For magnesium and sulfur, the redistributions of both elements were similar (Figure 19c, d). The scanings showed higher values at near the casting surface and then gradually decreased. In the case of magnesium, the values on the far side of the casting surface were close to the melt average (0.035%). On the other hand, the values of sulfur were higher than the melt average (0.017%), as there were influenced by the diffusion of sulfur from the core to the casting. The occurrence of the magnesium and sulfur-rich area was due to formation of the MgS (desulfurizing reaction). According to Voronova<sup>20</sup> the reactions and the corresponding change in free energy are,



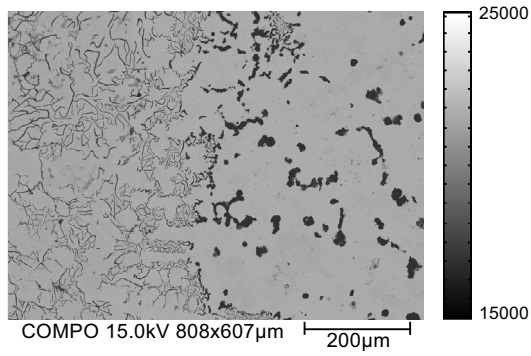
where  $T$  is the temperature. This is not to be confused with magnesium depletion via oxidation. As oxidation forms MgO which then leave the iron melt similar to the fading effect after spheroidization (*i.e.*, Mg treatment) before

pouring. In addition, there were some high signal value for magnesium and sulfur throughout the readings. Presumably, these readings were corresponding to MgS particles. No segregation was observed at the LG-SG transition.

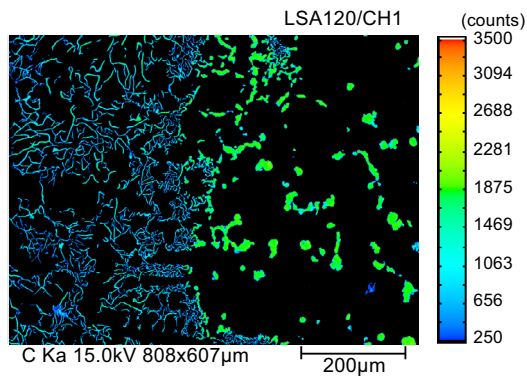
## Conclusions

This study demonstrates an approach for creating the Functionally-Graded Materials over the different in structures and properties between LG and SG. The hybridization was done by placing the sulfur-bearing cores where the LG were needed. Followings are key findings.

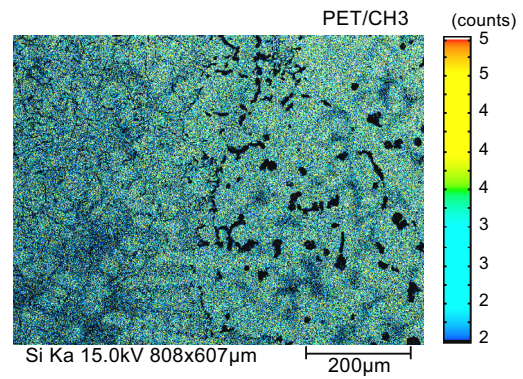
- It is seen that the sulfurization method worked well with the hypoeutectic iron where the hyper-eutectic showed a difficulty of graphite flotation.
- Graphite shape factors (*e.g.*, roundness, circularity, aspect ratio) showed different values between the LG layer and SG structure. It was viable to use the graphite shape factors to quantify the microstructure across the LG-SG transition.
- The thickness of LG layer increased with the level of sulfur in cores until reaching the highest value at 6.6 and 8.8 wt%S for mixed and coated cores, respectively. Higher level of sulfur did not yield thicker LG layer due to the chilling effect of the cores. The surface quality from the coated cores was superior to the mixed counterpart.
- The EPMA revealed that both magnesium and sulfur in the casting were rich at the adjacent to the cores. Magnesium and sulfur were tied up by forming MgS in the area.



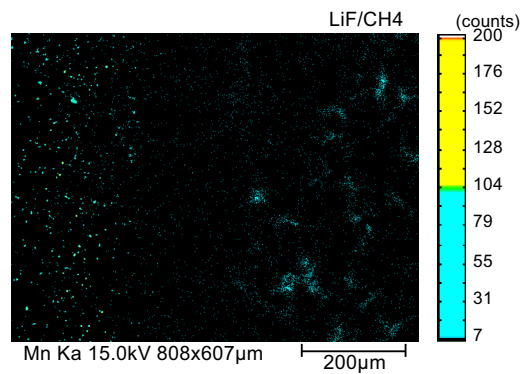
a) Test field



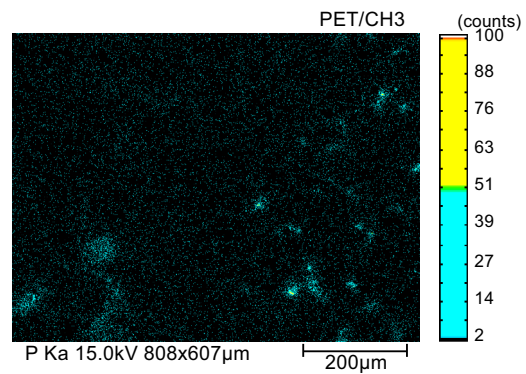
b) Carbon



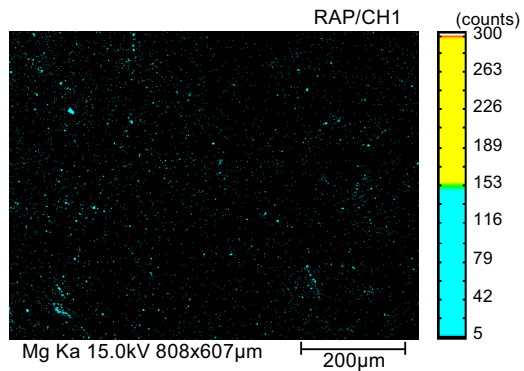
c) Silicon



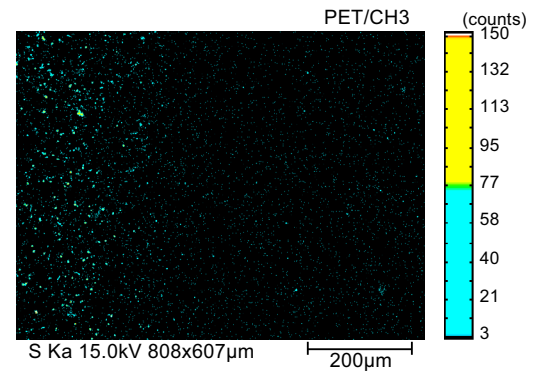
d) Manganese



e) Phosphorus



f) Magnesium



g) Sulfur

Figure 18. Electron Probe Microanalysis (EPMA) element mappings of the LG-SG transition area (8.8 wt%S-coated core).

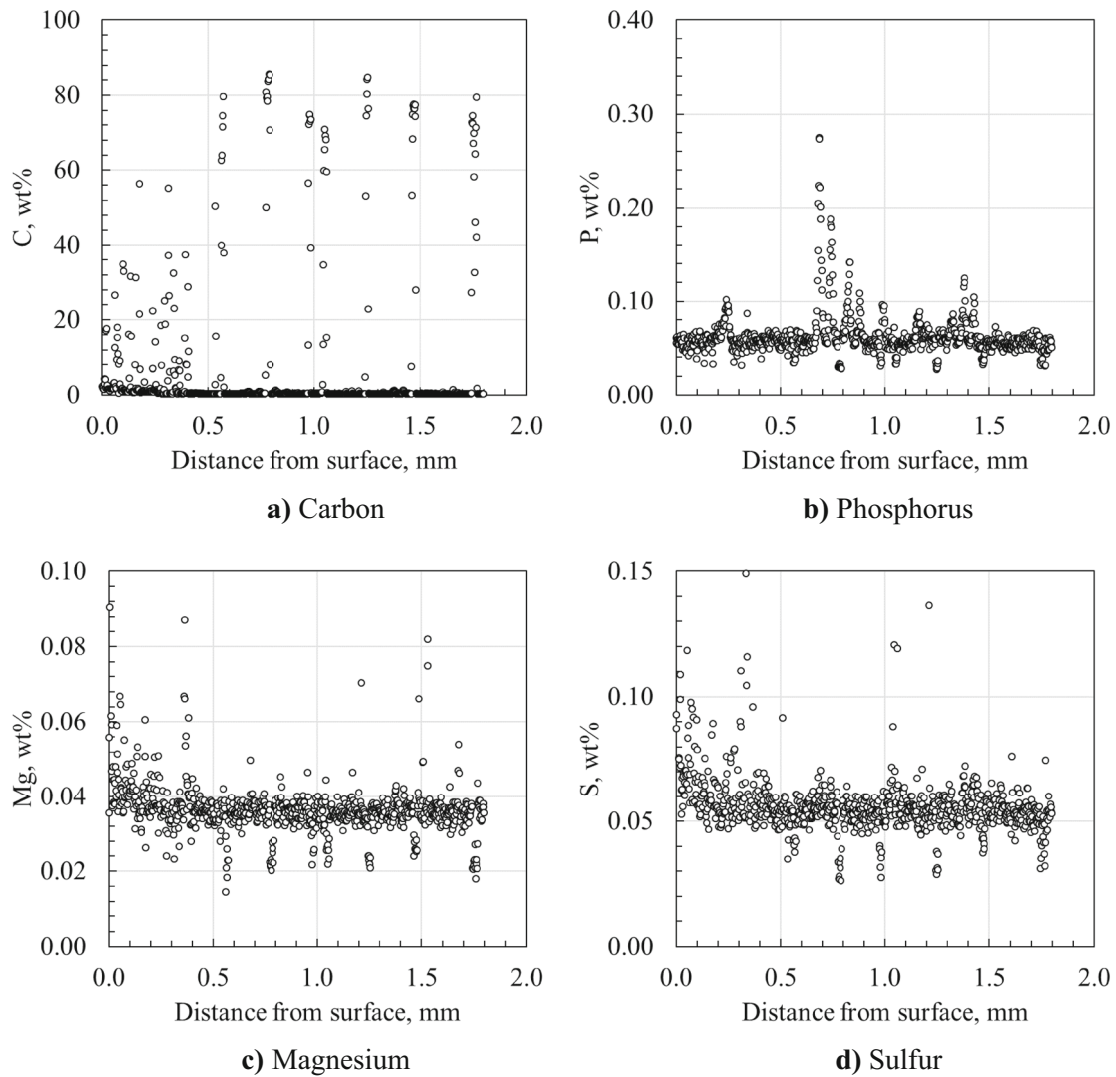


**Figure 19. Line scanings of the LG-SG transition area using EPMA.**

### Acknowledgement

This work was supported by (i) Suranaree University of Technology (SUT), (ii) Thailand Science Research and Innovation (TSRI), and (iii) National Science, Research and Innovation Fund (NSRF).

### REFERENCES

1. S. Boonmee, D. Stefanescu, Effect of casting skin on fatigue properties of CG iron. *Inter Metalcast* **7**, 15–26 (2013). <https://doi.org/10.1007/BF03355550>
2. C. Labrecque, M. Gagné, P. Cabanne et al., Comparative study of fatigue endurance limit for 4 and 6 mm thin wall ductile iron castings. *Inter Metalcast* **2**, 7–17 (2008). <https://doi.org/10.1007/BF03355424>
3. S. Boonmee, B. Gyasi, D.M. Stefanescu, Casting skin of compacted graphite iron part I: evaluation and mechanism for formation. *AFS Trans.* **118**, 205–216 (2010)
4. S. Boonmee, D.M. Stefanescu, Casting skin management in compacted graphite iron part II: effect of mold coating and section thickness. *AFS Trans.* **118**, 217–226 (2010)
5. N. Ivan, M. Chisamera, I. Riposan, Mold coatings to reduce graphite degeneration in the surface layer of ductile iron castings. *Inter Metalcast* **6**, 61–70 (2012). <https://doi.org/10.1007/BF03355539>
6. D. Dhaneswara, B. Suharno, R.D.S. Ariobimo et al., Effect of coating layer of sand casting mold in thin-walled ductile iron casting: reducing the skin effect formation. *Inter Metalcast* **12**, 362–369 (2018). <https://doi.org/10.1007/s40962-017-0173-4>
7. S.N.A.B. Safri, M.T.H. Sultan, M. Jawaid, *Damage analysis of glass fiber reinforced composites, composites science and engineering* (Woodhead Publishing, Sawston, 2019), pp.133–147
8. R.M. Mahmood, E.T. Akinlabi, Types of functionally graded materials and their areas of application, in

*Functionally Graded Materials*. (Springer, Cham, 2017), pp.9–21

9. V. Kapsali, *Biomimetics for designers: applying nature's processes and materials in the real world*, Thames & Hudson, Ltd. (2021)
10. A.D. Pradeep, T. Rameshkumar, Review on centrifugal casting of functionally graded materials. *Mater. Today Proc.* **45**, 729–734 (2021)
11. K. Rane, M. Beining, S. Behera et al., Sand casting of surface alloyed butterfly valve with improved hardness and corrosion resistance by incorporating metal powders in-mold coatings. *Inter Metalcast* **16**, 359–369 (2022). <https://doi.org/10.1007/s40962-021-00609-4>
12. M.K. El Fawkhry, T. Mattar, Influence of diffusion and wetting on the sic reinforcement of the cast surface of low alloy steel. *Inter Metalcast* **12**, 139–147 (2018). <https://doi.org/10.1007/s40962-017-0151-x>
13. T. Wróbel, N. Przyszlak, A. Dulcka, Technology of alloy layers on surface of castings. *Inter Metalcast* **13**, 604–610 (2019). <https://doi.org/10.1007/s40962-018-00304-x>
14. A.B. Malizio and R.W. Jennings (1989). U.S. Patent No. 4832084
15. F. Marti, S.I. Karsay, Localized flake graphite structure as a result of a reaction between molten ductile iron and some components of the mold. *AFS Trans.* **87**, 221–226 (1979)
16. S. Nasu, S. Fujita, N. Furusato et al., Effect of casting skin condition on fatigue strength of gray cast iron. *Inter Metalcast* **11**, 155–161 (2017). <https://doi.org/10.1007/s40962-016-0109-4>
17. S.N. Lekakh, J. Qing, V.L. Richards, Investigation of cast iron processing to produce controlled dual graphite structure in castings. *AFS Trans.* **120**, 297–306 (2012)
18. S. Boonmee, N. Mai-Ngam, On the development of the dual graphite iron. *Materials Today: Proceedings* **5**(3), 9264–9271 (2018)
19. A. Kutz, P. Martin, A. Bührig-Polaczek, Microstructural adjustment of the degenerated graphite layer in ductile iron for targeted evaluation on the fatigue properties. *Inter Metalcast* **14**, 1183–1194 (2020). <https://doi.org/10.1007/s40962-020-00455-w>
20. N.A. Voronova, *Desulfurization of hot metal by magnesium*, iron and steel society (1983)

**Publisher's Note** Springer Nature remains neutral with regard to jurisdictional claims in published maps and institutional affiliations.

Springer Nature or its licensor (e.g. a society or other partner) holds exclusive rights to this article under a publishing agreement with the author(s) or other rightsholder(s); author self-archiving of the accepted manuscript version of this article is solely governed by the terms of such publishing agreement and applicable law.